PHYSICAL REVIEW E **70**, 021405 (2004)

Brownian dynamics simulations of Laponite colloid suspensions

G. Odriozola,* M. Romero-Bastida,† and F. de J. Guevara-Rodríguez‡
Programa de Ingeniería Molecular, Instituto Mexicano del Petróleo, Eje Central Lázaro Cárdenas 152,
07730 México, Distrito Federal, Mexico

(Received 29 January 2004; published 31 August 2004)

Colloidal suspensions of Laponite clay platelets are studied by means of Brownian dynamics simulations. The platelets carry discrete charged sites which interact via a Yukawa potential. As in the paper by S. Kutter *et al.* [J. Chem. Phys. **112**, 311 (2000)], two models are considered. In the first one all surface sites are identically negative charged, whereas in the second one, rim charges of opposite sign are included. These models mimic the behavior of the Laponite particles in different media. They are employed in a series of simulations for different Laponite concentrations and for two values of the Debye length. For the equilibrium states, the system structure is studied by center-to-center and orientational pair distribution functions. Long-time translational and rotational self-diffusion coefficients are computed by two different methods, which yield very similar results.

DOI: 10.1103/PhysRevE.70.021405 PACS number(s): 61.20.Ja, 61.20.Lc

I. INTRODUCTION

Clay colloidal suspensions appear in several industrial processes. Examples are found in the ceramic, paint, cosmetic, and petroleum industries, among others [1,2]. In many of their applications, the interest in them is driven by the diversity of behaviors they show. These go from a Newtonian liquid up to a viscoelastic gel; they may even form a flocculated dispersion, depending on their type, size, shape, concentration, and medium composition [3–6]. Hence, understanding their behavior is both a challenge and a necessity.

Clays are lamellar mineral crystals. In particular, Laponite particles are three-layer synthetic clays composed of a central magnesium sheet sandwiched by two silica sheets [7,8]. This structure forms thin platelet-shaped lamellas of diameters close to 25 nm and thicknesses of 1 nm, which can be separated to form a water dispersion. Due to existing isomorphous substitutions of a fraction of divalent magnesium ions by monovalent lithium ions, the net charge of the Laponite flat surface is negative. The edge surfaces of the Laponite particles, however, behave quite differently. Here, the tetrahedral silica sheets and the octahedral magnesia sheets are disrupted, leading to the adsorption of specific ions which rule the surface charge. Hence, depending on the media composition, the edge surface may be negatively or positively charged.

We should mention here that the regular size and shape that characterizes this synthetic clay make it very convenient for experimental studies. In fact, lately there has been a lot of experimental work on Laponite dispersions by means of scattering and rheological techniques [5–7,9,10]. On the other hand, although the one-dimensional swelling of hydrated clays has been very well studied by computer simulations [11–14], a theoretical description of their suspensions is not very developed. This is at least partially due to the fact that the highly anisotropic shape of the particles makes the interparticle potential extremely complicated. There are, however, three very interesting theoretical works by Dijkstra *et al.* and Kutter *et al.* [15,16]. In the first two, the Laponite particles are modeled by platelets which carry a constant electrostatic quadrupole moment. This approach, although crude, was capable of predicting a sol-gel transition, in good agreement with experimental observations. The third work, a molecular dynamics study, presents a much more realistic model, where the platelets carry a given number of charged sites homogeneously distributed over their surfaces. In addition, the particles are assumed to be dispersed in water, and hence, the screened electrostatic interaction is modeled by a Yukawa potential. Another important feature of this model is that it allows the study of the effect of rim charges of a different nature than the surface ones. In this way, the flat and edge surfaces of the Laponite particles are modeled.

In this paper, we further study the behavior of the Laponite suspensions by means of Brownian dynamics (BD) considering a model similar to the one employed by Kutter *et al.*. This technique has the advantage of considering the effect of the solvent, although we still do not consider the much more complicated hydrodynamic interactions between platelets. Hence, the dynamical and transport properties have a better physical grounding. This allows us to study the behavior of the diffusion coefficients as a function of the platelet concentration and the Debye length. Nevertheless, the accuracy of the obtained diffusion coefficients is expected to decrease with increasing platelet concentration, due to the neglect of hydrodynamic interactions. On the other hand, our model impedes platelet interpenetration by considering a large number of short-ranged repulsive sites. As we will show, this plays an important role in the structure of those systems that show a tendency to aggregate.

The paper is organized as follows. The model for the Laponite particles and the implementation of the BD simulation is described in Sec. II. Section III is devoted to the presentation and discussion of the results. In Sec. IV we discuss the implications on the local structure and on the self-diffusion coefficients of the pair potential as a function of the number of charged sites. Finally, in Sec. V we present our conclusions.

---

*Electronic address: godriozo@imp.mx

†Electronic address: mromerob@imp.mx, rbm@xanum.uam.mx

‡Electronic address: fguevara@imp.mx

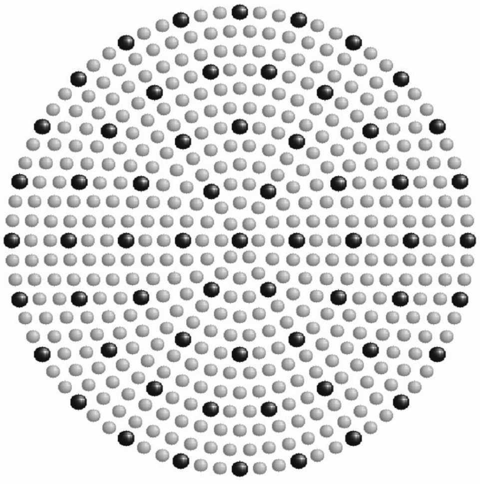

FIG. 1. Bead model formed by $N_T=469$ spheres of diameter $\sigma_{\parallel}$ for evaluating the Laponite-Laponite interaction energy. As can be seen, the arrangement geometry is a disk of diameter $\sigma_{\perp}=25$ nm and thickness $\sigma_{\parallel}=1$ nm.

II. THE MODEL

A. Pair potential

As mentioned in the preceding section, Laponites are synthetic clay particles with a highly regular geometry similar to a disk of diameter $\sigma_{\perp}=25$ nm and thickness $\sigma_{\parallel}=1$ nm, which have the following unit cell formula: $\mathrm{Na}_{0.7}^{+}[(\mathrm{Si}_8\mathrm{Mg}_{5.5}\mathrm{Li}_{0.3})\mathrm{O}_{20}(\mathrm{OH})_4]^{-0.7}$. When dispersed by water, the sodium ions are released from their surface, leading to a net surface charge of $Q_T\approx -700$ e, and hence, to 700 charged sites. Hence, a first model for the Laponite is given by distributing this charge over its surface (model *A*). For acid conditions, however, due to the absorption of certain specific ions on the particles edges, they may also show a local positive ring charge whose value may reach 10% of the absolute value of their net charge, depending on the *p*H of the suspension. In this case, we assume a negative charge $Q_-\approx 1.1Q_T$ and a positive charge $Q_+\approx -0.1Q_T$ uniformly distributed on the flat and edge surface of the Laponite particle, respectively (model *B*).

To obtain the thermodynamic and transport properties of such a suspension we modeled the Laponites by rigid arrangements of $N_T(=469)$ spherical particles of diameter $\sigma_{\parallel}$, as shown in Fig. 1. In this way, the Laponite-Laponite interaction energy is evaluated as the sum of single site-to-site Yukawa type interactions, namely,

$$\phi_{\alpha\beta}^{(Y)} \equiv \sum_{i=1}^{N_T}\sum_{j=1}^{N_T} \frac{q_{i\alpha}q_{j\beta}}{\epsilon r_{i\alpha j\beta}} \exp(-\kappa_D r_{i\alpha j\beta}), \tag{1}$$

where $\alpha(\neq\beta)$ is an index associated to the Laponites, $\epsilon=78$ is the water dielectric constant at room temperature, $q_{i\alpha}$ is the electric charge assigned to each bead, $r_{i\alpha j\beta}=|\boldsymbol{r}_{i\alpha}-\boldsymbol{r}_{j\beta}|$ is the site-to-site distance, and $\boldsymbol{r}_{i\alpha}$ is the vector located in the center of each charge. Of course, the net charge of each Laponite platelet is $\sum_{i=1}^{N_T} q_{i\alpha}=Q_T$. Finally, $\kappa_D=1/\lambda$ is the Debye screening parameter and λ the Debye length. They are given by

$$\kappa_D^2 = 1/\lambda^2 = \frac{4\pi(n_+z_+^2+n_-z_-^2)e^2}{\epsilon k_B T}, \tag{2}$$

where n_+, n_-, z_+, and z_- are the concentrations and valences of positive and negative ions and k_BT is the thermal energy.

At this point, we should mention that Kutter *et al.* have used several rigid hexagonal bead models to implement the interaction between these types of particles. They checked the form factor [defined by Eq. (2.6) of Ref. [15]] and concluded that a 61 bead discrete model provides a good approach for the form factor of a solid disk. They also performed a test to study the effect of discretizing the charge Q_T on the surface of spherical particles. For this purpose, they carried out two molecular dynamic simulations, one for a set of spheres with their charge continuously distributed on their surface and the other for the same set but with discretized charge, and calculated the radial distribution function for each case. They observed a good agreement between the radial distribution functions of both systems for a discretization of 61 sites and for the same total charge Q_T. They concluded that the discrete representation of the charge Q_T through 61 sites is a good approach to the continuous distribution of the charge Q_T on the surface of the particles. Nevertheless, it is important to emphasize the following facts: the radial distribution function is not very sensitive to changes in the charge discretization over spherical particles due to their symmetry and the Debye length employed for performing the test (58.9 nm) is much larger than those used for the study itself ($\sim$9, 3, and 1 nm). Hence, there is not any guarantee that systems having other Debye lengths and particles with other geometries such as platelets should also behave properly if their particles are discretized in a similar fashion. As a first step, however, we also assume that a 61 site charge discretization may approach the 700 site discretization of the charge Q_T on the surface of the platelets. Thus, the subset of beads where we assign the electric charge $q_{i\alpha}=Q_T/61$ is shown in Fig. 1 as dark spheres, whereas the light ones are assigned $q_{i\alpha}=0$. In this way, we have defined model *A* of a Laponite particle characterized by a completely repulsive potential, i.e., for a high hydroxyl concentration.

In order to take into account the effect of the positive electric charges on the Laponite edges that appear in acid media, we define model *B* by

$$q_{i\alpha} = \begin{cases} Q_+/N_+ & \text{dark spheres on the edge,} \\ Q_-/N_- & \text{inner dark spheres,} \\ 0 & \text{light spheres,} \end{cases} \tag{3}$$

where $N_+=24$ and $N_-=37$. Here, we define the number of charged sites by $N_q\equiv N_++N_-$.

This last model may lead to particle interpenetrations and numerical instabilities as a consequence of the attractive interactions between the positive and negative charges of different particles. Thus, in order to avoid particle interpenetration we imposed a short-range potential given by

$$\phi^{(S)}_{\alpha\beta} \equiv \sum_{i=1}^{N_T}\sum_{j=1}^{N_T} \frac{C}{r^6_{i\alpha j\beta}}. \tag{4}$$

Here, the C value is adjusted in such way that the total interaction energy between a positive and negative site at contact (1 nm) is around 1 k_BT, where k_B is the Boltzmann's constant and $T=300$ K is the temperature. Hence, the total interaction energy in a N platelets system is given by

$$\phi \equiv \sum_{\alpha=1}^{N-1}\sum_{\beta=\alpha+1}^{N} \left(\phi^{(Y)}_{\alpha\beta} + \phi^{(S)}_{\alpha\beta}\right), \tag{5}$$

whereas the net force acting on site i of platelet α is

$$\boldsymbol{F}_{i\alpha} = -\sum_{\beta=1}^{N}\sum_{j=1}^{N_T} \boldsymbol{\nabla}_{i\alpha j\beta}\left(\frac{q_{i\alpha}q_{j\beta}\exp(-\kappa_D r_{i\alpha j\beta})}{\epsilon r_{i\alpha j\beta}} + \frac{C}{r^6_{i\alpha j\beta}}\right) \tag{6}$$

and the net force acting on the center of mass (c.m.) of platelet α is

$$\boldsymbol{F}_\alpha = \sum_{i=1}^{N_T} \boldsymbol{F}_{i\alpha}. \tag{7}$$

Finally, the net torque acting on the c.m. of platelet α reads

$$\boldsymbol{T}_\alpha = \sum_{i=1}^{N_T} (\boldsymbol{r}_{i\alpha} - \boldsymbol{R}_\alpha) \times \boldsymbol{F}_{i\alpha}, \tag{8}$$

where $\boldsymbol{R}_\alpha$ is the c.m. position of platelet α.

B. Brownian dynamics algorithm

In an ordinary BD simulation, the evolution of the c.m. and the orientation of a nonspherical particle is given by the integration of the appropriate set of Langevin equations. In the simplest case of spherical particles, this methodology was developed and implemented by Ermak [17]. In this work, the methodology is adapted for updating the c.m. positions of the platelets. To update the orientation of the platelets, however, there are two equivalent methodologies that simply differ on the selection of the reference frame. The first one uses the body reference frame to describe the BD. This methodology is, for example, employed by Löwen [18] for a set of spherocylinders. The other one uses a fixed reference frame to solve the equations of motion. This last is employed by Heyes [19–21] for a set of particles modeled by a linear arrangement of beads. In this work we adopted the first methodology, and thus for each platelet, the c.m. position is decomposed into a parallel and two perpendicular components to the axial axis through

$$\boldsymbol{R}^{(s)}(t) = \boldsymbol{A}(t)\cdot\boldsymbol{R}^{(b)}(t), \tag{9}$$

where $\boldsymbol{A}(t)$ is the rotation matrix associated to the corresponding platelet. This matrix relates the two descriptions of the same object, i.e., the c.m. vector. The descriptions of vector $\boldsymbol{R}(t)$ are denoted by (s) and (b) corresponding to system and body references, respectively. Moreover, the axes of each body-reference frame are parallel to the principal axes of the corresponding platelet. In particular, the z axis is along the axial axis of the particle and so, the description of vector $\boldsymbol{R}(t)$ in the body-reference frame turns:

$$\boldsymbol{R}^{(b)}(t) = (R_{\perp_x}, R_{\perp_y}, R_\parallel). \tag{10}$$

The same procedure is done for the total force $\boldsymbol{F}(t)$ acting on the c.m. of the platelet due to the interactions with the other platelets. Hence, after obtaining $\boldsymbol{F}^{(s)}(t)$ by means of Eq. (7), relationship

$$\boldsymbol{F}^{(b)}(t) = \boldsymbol{A}^{-1}(t)\cdot\boldsymbol{F}^{(s)}(t) \tag{11}$$

is applied for obtaining $\boldsymbol{F}^{(b)}(t) = (F_{\perp_x}, F_{\perp_y}, F_\parallel)$. Thus, for a finite time step Δt, the evolution of the platelet's c.m. is given by

$$\Delta R^{(b)}_*(t+\Delta t) \approx \frac{D^{T,0}_*}{k_BT} F^{(b)}_*(t)\Delta t + \Delta R^{(g)}_*(\Delta t), \tag{12}$$

where $* = \perp_x, \perp_y$, and $\parallel$. In this equation, $D^T_{\perp_x} = D^T_{\perp_y}$ and $D^T_\parallel$ are the free translational diffusion coefficients of the platelets whose values are discussed in the following section. In the same equation, $\Delta R^{(g)}_*(\Delta t)$ is the random displacement of the particle c.m. that appears due to the solvent transference of momenta. This random displacement has a Gaussian distribution with zero mean and variance

$$\langle|\Delta R^{(g)}_*(\Delta t)|^2\rangle = 2D^{T,0}_*\Delta t. \tag{13}$$

Next, the c.m. position is updated by

$$\boldsymbol{R}^{(s)}(t+\Delta t) = \boldsymbol{R}^{(s)}(t) + \boldsymbol{A}(t)\cdot\Delta\boldsymbol{R}^{(b)}(t+\Delta t). \tag{14}$$

Note that in Eq. (14) we use the rotation matrix $\boldsymbol{A}(t)$ instead of $\boldsymbol{A}(t+\Delta t)$. This is because we split the complex evolution of the platelet in two parts. The first part, previously explained, accounts only for the pure c.m. translation. The second, to be explained, accounts for the pure rotation around corresponding Laponites' axes having their c.m. positions fixed. Hence, this procedure updates all matrixes $\boldsymbol{A}$.

For this purpose, the torque $\boldsymbol{T}(t)$ is calculated by means of Eq. (8) and is decomposed to its corresponding body reference components using

$$\boldsymbol{T}^{(b)}(t) = \boldsymbol{A}^{-1}(t)\cdot\boldsymbol{T}^{(s)}(t). \tag{15}$$

Thus, for the same finite time step Δt and a given platelet, the evolution of each angle around the corresponding platelet's principal axis are given by

$$\Delta\varphi_*(t+\Delta t) \approx \frac{D^{R,0}_*}{k_BT} T^{(b)}_*(t)\Delta t + \Delta\varphi^{(g)}_*(\Delta t), \tag{16}$$

where the random angular displacement $\Delta\varphi^{(g)}_*(\Delta t)$ has a Gaussian distribution with zero mean and variance

$$\langle|\Delta\varphi^{(g)}_*(\Delta t)|^2\rangle = 2D^{R,0}_*\Delta t. \tag{17}$$

The angles $\Delta\varphi_{\perp_x}, \Delta\varphi_{\perp_y}$, and $\Delta\varphi_\parallel$ [Eq. (16)] are then employed for constructing the matrixes associated with the rotation around each platelet principal axis. These matrixes read

$$A_{\perp_x}(t+\Delta t) = \begin{pmatrix} 1 & 0 & 0 \\ 0 & \cos\Delta\varphi_{\perp_x} & -\sin\Delta\varphi_{\perp_x} \\ 0 & \sin\Delta\varphi_{\perp_x} & \cos\Delta\varphi_{\perp_x} \end{pmatrix},$$

$$A_{\perp_y}(t+\Delta t) = \begin{pmatrix} \cos\Delta\varphi_{\perp_y} & 0 & \sin\Delta\varphi_{\perp_y} \\ 0 & 1 & 0 \\ -\sin\Delta\varphi_{\perp_y} & 0 & \cos\Delta\varphi_{\perp_y} \end{pmatrix},$$

$$A_{\parallel}(t+\Delta t) = \begin{pmatrix} \cos\Delta\varphi_{\parallel} & -\sin\Delta\varphi_{\parallel} & 0 \\ \sin\Delta\varphi_{\parallel} & \cos\Delta\varphi_{\parallel} & 0 \\ 0 & 0 & 1 \end{pmatrix}. \qquad (18)$$

Given an arbitrary vector $\boldsymbol{u}$ fixed in the system-reference frame, the rotational matrix $\Delta A \approx A_{\perp_x} A_{\perp_y} A_{\parallel}$ relates its representation in the body reference at time t with its representation in the body reference at time $t+\Delta t$ by means of

$$\boldsymbol{u}^{(b)}(t) = \Delta\boldsymbol{A}(t+\Delta t)\cdot\boldsymbol{u}^{(b)}(t+\Delta t). \qquad (19)$$

Substituting the definition of the rotational matrix at time t, Eq. (9), into Eq. (19), the updating rule for the rotational matrix $\boldsymbol{A}$ to time $t+\Delta t$ is found to be

$$\boldsymbol{A}(t+\Delta t) = \boldsymbol{A}(t)\cdot\Delta\boldsymbol{A}(t+\Delta t). \qquad (20)$$

It is important to mention that the previous definition of matrix ΔA will induce an error since the matrices $A_{\perp_x}, A_{\perp_y}$, and $A_{\parallel}$ are not commutable. Nevertheless, the mean error becomes negligible for a small enough value of the time step Δt used during a long run of the BD simulation [20,22].

Finally, and similarly to the above described translational case, $D^R_{\perp_x} = D^R_{\perp_y}$ and $D^R_{\parallel}$ are the free rotational diffusion coefficients of the platelets. In the following section, we focus on them in order to complete the methodology.

C. Free diffusion coefficients

The BD simulation technique requires the knowledge of the free diffusion coefficients of the considered particles. In the case of a spherical particle the free translational diffusion coefficient is given by Einstein's identity and the Stokes law value, i.e., $D_0^T = k_B T/3\pi\eta\sigma$, where σ is particle diameter and η is the solvent viscosity ($\eta \approx 1.002$ cP for water at room temperature [23]). In this simple case, the free rotational diffusion coefficient D_0^R is directly related to the free translational diffusion coefficient by $\sigma^2 D_0^R/3 = D_0^T$ [24]. These coefficients are used further in this subsection to normalize the free diffusion coefficients of the particles of interest.

As previously mentioned, the Laponite platelets are composed of N_T identical spheres which form a rigid arrangement. This is illustrated in Fig. 1. Nevertheless, this bead model is employed exclusively to evaluate the configuration energy. From a hydrodynamic point of view, the Laponite platelets are modeled by oblate ellipsoids with diameters $\sigma_{\parallel}$ and $\sigma_{\perp}$. These diameters are parallel and perpendicular to the axial axis, respectively. For such particles, its aspect radio is usually defined by $\kappa \equiv \sigma_{\perp}/\sigma_{\parallel}$, since the hydrodynamic theory leads to analytic expressions for the diffusion coefficients as a function of it [25,26]. They read

$$D_{\perp}^{T,0}/D_0^T = \frac{3}{8}\left[\frac{(3\kappa^2-2)S-1}{\kappa^2-1}\right],$$

$$D_{\parallel}^{T,0}/D_0^T = \frac{3}{4}\left[\frac{(\kappa^2-2)S+1}{\kappa^2-1}\right],$$

$$D_{\perp}^{R,0}/D_0^R = \frac{3}{2}\left[\frac{(\kappa^2-2)S+1}{\kappa^4-1}\right],$$

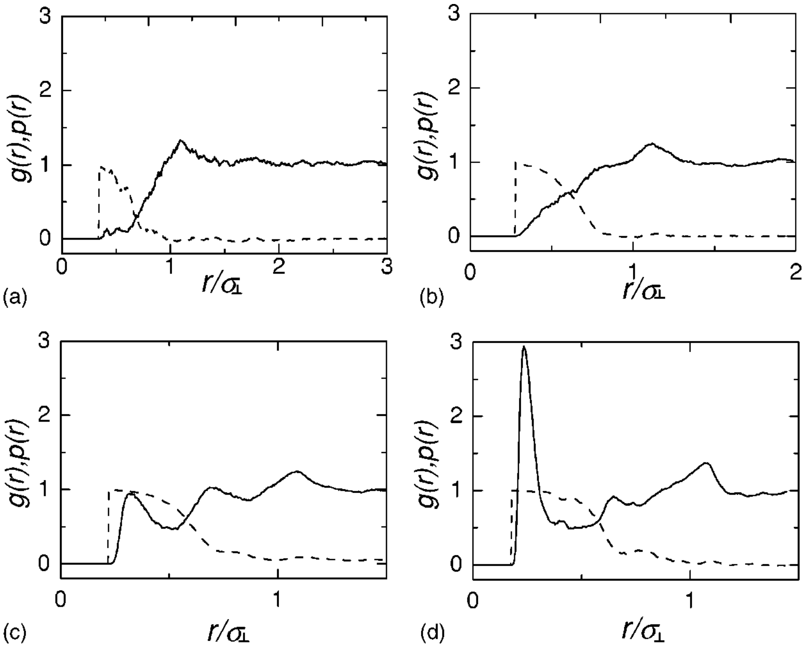

FIG. 2. Radial distribution function (continuous line) and angular distribution function (dashed line) for model A, $\lambda = 1$ nm and (a) $\rho = 0.01$, (b) 0.05, (c) 0.09, and (d) 0.13.

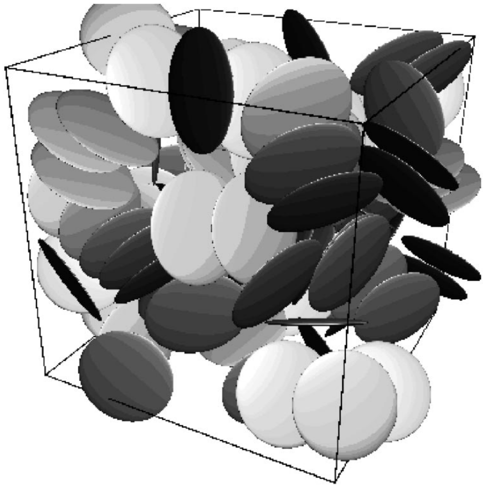

FIG. 3. Typical configuration for model *A*, $\lambda = 1$ nm, and $\rho = 0.09$.

$$D_{\parallel}^{R,0}/D_0^R = \frac{3}{2}\left[\frac{\kappa^2 S - 1}{\kappa^2(\kappa^2 - 1)}\right], \tag{21}$$

where

$$S = (\kappa^2 - 1)^{-1/2}\arctan\left(\sqrt{\kappa^2 - 1}\right). \tag{22}$$

In Eq. (21), $D_{\perp}^T$ and $D_{\parallel}^T$ are free translation diffusion coefficients that correspond to displacements that are perpendicular and parallel to the particle axial axis, respectively. Similarly, $D_{\perp}^R$ and $D_{\parallel}^R$ are free rotation diffusion coefficients that correspond to angular displacements around axes that are perpendicular and parallel to the particle axial axis, respectively. Naturally, the free diffusion coefficients associated to our Laponite model corresponds to $\kappa = 25$. Thus, the methodology for the BD simulation that was introduced in the preceding section is completed.

III. RESULTS

A. Simulation details

The computations were performed by considering the Laponite models previously described. All systems studied consisted of $N = 100$ platelets, which were randomly located and oriented in a cubic simulation cell of volume *V*. For avoiding platelets to be interpenetrated in the initial configuration, we resituate those that overlap with others. In order to identify them a full site to site test was performed. The temperature was chosen to be $T = 300$ K and the solvent viscosity $\eta_0 = 1.002$ cP, which corresponds to water under this temperature. The volume fraction ρ (defined as NV_p/V, where $V_p = \pi\sigma_{\perp}^2\sigma_{\parallel}/4$ is the platelet volume) was varied in the range [0.01, 0.15] in steps of 0.02 and the Debye length λ was fixed to 1 and 3 nm. This makes 16 simulations for each model. Periodic boundary conditions were considered and a cutoff equal to half the edge size of the cell was imposed. The particle trajectories were generated according to the algorithm defined in Sec. II B. Energy was monitored in the progress towards equilibrium.

For each condition set an equilibration run of 10^5 steps was performed, during which the value of the time step Δt was adjusted in such a way that the mean-square displacement of the Laponites' c.m. positions was approximately 0.01 nm^2. The obtained time-step mean values after equilibration range in (0.003, 0.004) ns in all cases except for model *B*, with $\lambda = 3$ nm and $\rho = 0.13$ and 0.15 which were around 0.0015 ns. It is important to mention that the adjustment of the time-step was carried out only during the equilibration process. During the formal run of 2×10^5 steps, the value of the time step remains fixed and equal to the mean value previously found.

B. Structural properties

The quantitative characterization of the local structure of the suspension is provided by two different pair distribution

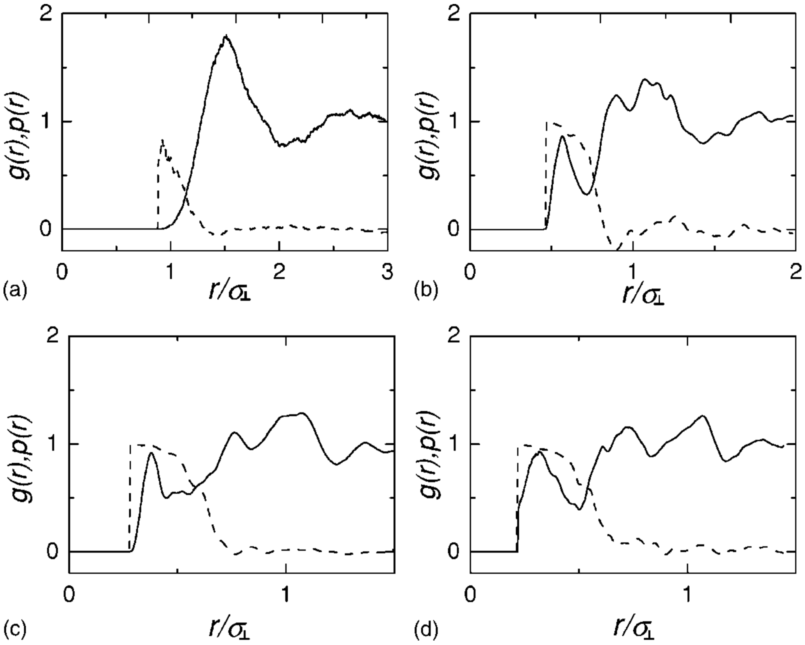

FIG. 4. Radial distribution function (continuous line) and angular distribution function (dashed line) for model *A* with $\lambda = 3$ nm and volume fraction (a) $\rho = 0.01$, (b) 0.05, (c) 0.09, and (d) 0.13.

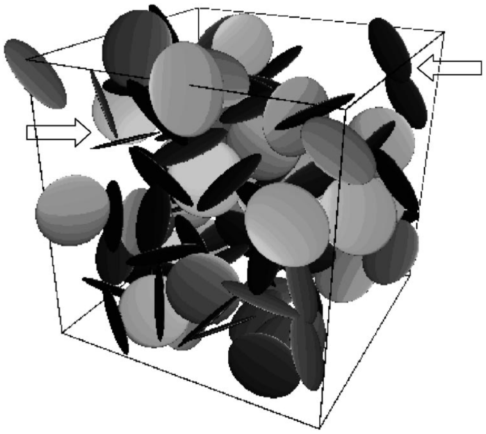

FIG. 5. Typical configuration for model *B* with $\rho=0.05$ and $\lambda=1$ nm. Arrows show a T-shaped (left) and PPO (right) configuration.

functions. One of them is the radial distribution function $g(r)$ [27] which describes the correlations between the c.m. of a platelet with the c.m. of another at the radial distance r. The second one is the angular distribution function, which is obtained by taking the statistical average of the second Legendre polynomial for a fixed distance $r=|\boldsymbol{R}_\alpha-\boldsymbol{R}_\beta|$ between the c.m. of two platelets, namely,

$$p(r) \equiv \left\langle \frac{1}{2}(3\cos^2\theta(r)-1)\right\rangle, \tag{23}$$

where $\langle\cdots\rangle$ means a statistical average over all pairs. Here, $\theta(r)$ is the angle between the normals $\boldsymbol{n}_\alpha$ and $\boldsymbol{n}_\beta$ of platelets α and β. In this way, when neighboring platelets are nearly parallel the value of $p(r)$ is close to 1, whereas for a T-shaped configuration it is close to $-1/2$.

The results for $g(r)$ and $p(r)$ corresponding to model *A*, $\lambda=1$ nm as a function of ρ are presented in Fig. 2. For the lowest values of ρ the suspension behaves almost as an isotropic gas since the corresponding radial and angular distribution functions are structureless. It is to be noted that $p(r)$ indicates a preferential parallel orientation of platelets for c.m. distances of the order of the platelet radius or less, although these configurations are quite rare because of the repulsion between sites. In fact, the parallel orientation is seen for all ρ considered, but its relative importance increases with it. Hence, with an increasing ρ value the structure gradually builds up, and is dramatically enhanced for not so high concentrations. In particular, for $\rho=0.09$, the system shows signatures of long range order corresponding to a structure of several parallel platelets, as is indicated by the three $g(r)$ peaks, which are equally separated by a distance close to $0.35\sigma_\perp$. A snapshot of a typical equilibrium configuration of this particular system is depicted in Fig. 3. As can be seen, the system is composed of several parallel local arrangements of platelets which are oriented in different directions, thus making the peak of $p(r)$ very close to 1, with decreasing height at larger separations. For even higher volume fractions, a large first peak in $g(r)$ is observed, indicating an increase of short range parallel order, whereas the other peaks have a much lower height.

Upon increasing λ from 1 to 3 nm the extended range of the repulsion between sites dramatically enhances the structure of the suspension, as can be seen in the results presented in Fig. 4. For example, at $\rho=0.01$ the structure is that of a simple fluid instead of a gas. In addition, the long range parallel order that for $\lambda=1$ nm sets in at $\rho=0.09$, now presents itself at the lower volume fraction of $\rho=0.05$. Indeed, for $\rho=0.09$ and $\rho=0.13$ an extra peak close to $1.4\sigma_\perp$ is obtained for the $g(r)$ function.

The influence of the rim charges on the structure and phase behavior is best understood by comparing the BD results for model *B* with those pertaining to model *A* under similar physical conditions. Inspection of typical configurations in this regime, such as those shown in Fig. 5, clearly

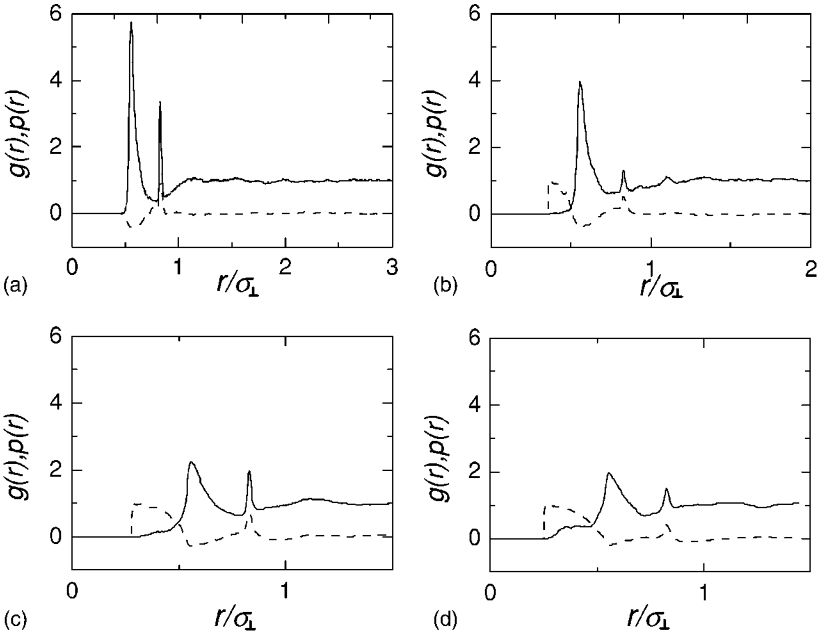

FIG. 6. Radial distribution functions (continuous line) and angular distribution function (dashed line) for model *B* with $\lambda=1$ nm and (a) $\rho=0.01$, (b) 0.05, (c) 0.09, and (d) 0.13.

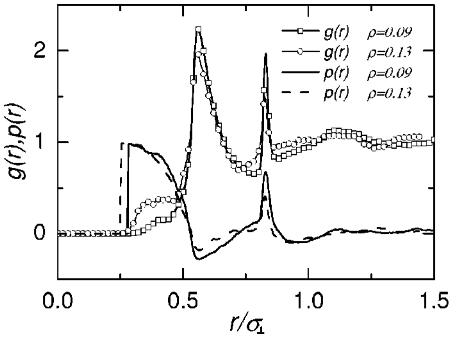

FIG. 7. Radial and angular distribution functions for model *B* with $\lambda=1$ nm and two different volume fractions around $\rho_{\min}$, which correspond to Fig. 6(c) and Fig. 6(d).

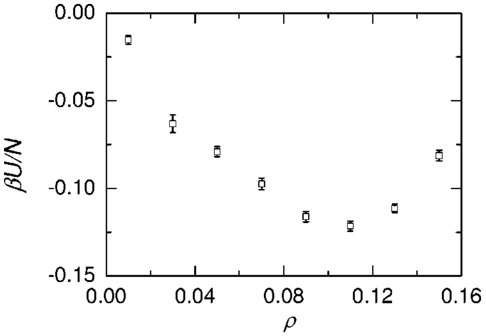

FIG. 8. Potential energy of model *B* with $\lambda=1$ nm as a function of volume fraction ρ.

points to the formation of clusters which are composed of two characteristic pair structures. In the first one the platelets tend to be perpendicular to each other forming a T-shaped pair configuration. In the second, the platelets tend to be in a parallel, partially overlapped (PPO) pair arrangement, with the centers separated by a distance close to $0.85\sigma_{\perp}$. It should be mentioned that this configuration is not observed if the noncharged sites that prevent the interpenetration of the platelets are not accounted. It is then not surprising that this particular arrangement is not reported in Ref. [15]. Both configurations are pointed out in Fig. 5. Other configurations involving more than two platelets, such as the house-of-cards type, are also clearly seen.

These qualitative observations are confirmed by a more quantitative analysis of the pair structure. Figure 6 shows the distribution functions for the same physical parameters as those of Fig. 2 for model *A*. The sharp first peak in $g(r)$ and the corresponding well of the $p(r)$ at a distance slightly larger than the platelet radius confirms the predominance of T-shaped pair configurations at short range. A second peak of lower but significant amplitude is present around $0.85\sigma_{\perp}$ for both radial distribution functions. Hence, this peak is a signature of the PPO arrangement previously mentioned. The fact that there is a very structured system at the lowest volume fraction 0.01 indicates that spontaneous aggregation is taking place. Hence, this behavior is also expected for even more diluted systems.

As the volume fraction is increased the amplitude of the peaks depicted in Fig. 6 drops. In addition, a parallel configuration appears at a separation lower than $\sigma_{\perp}/2$, which is detected by a small hump in $g(r)$ for the volume fraction $\rho=0.09$. The hump in $g(r)$ has a higher amplitude for the system with volume fraction $\rho=0.13$, as can be readily seen in the comparison of the distribution functions presented in Fig. 7. This configuration certainly originates from the packing of the platelets, since it is not energetically favored by the presence of the rim charges. Another way of visualizing this phenomenology is by plotting the potential energy of the system as a function of the volume fraction, as seen in Fig. 8. It is worth to notice in Fig. 8 that the volume fraction at which the potential energy has a minimum $\rho_{\min}$ is close to 0.11. The picture that emerges is that the T-shaped configurations always dominate the structure at all volume fraction values lower than $\rho_{\min}$, with a less significant contribution from the PPO configurations. For $\rho>\rho_{\min}$ the parallel con-

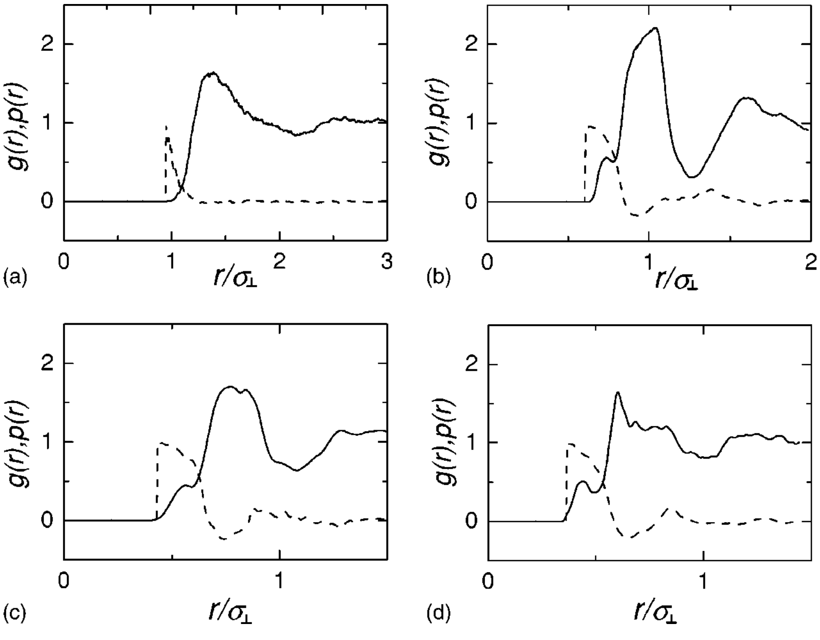

FIG. 9. Radial distribution function (continuous line) and angular distribution function (dashed line) for model *B* with $\lambda=3$ nm and volume fraction (a) $\rho=0.01$, (b) 0.05, (c) 0.09, and (d) 0.13.

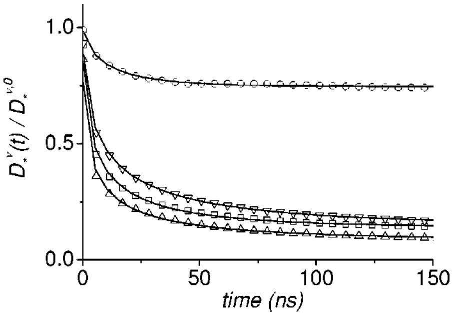

FIG. 10. Time-dependent SDC $D_{\perp}^{T}$ (square), $D_{\parallel}^{T}$ (up triangle), $D_{\perp}^{R}$ (down triangle), and $D_{\parallel}^{R}$ (circle) computed from the BD simulation. Solid, dashed, dotted, and dot-dashed lines are the corresponding fits. The particular case illustrated here corresponds to a model *B* system with volume fraction ρ=0.13 and λ=1 nm.

figurations are the only option to make the system more dense, thus increasing the value of the potential energy, as can be clearly seen.

Figure 9 presents the results for λ=3 nm. For this λ value the effect of the rim charges is to a great extent screened by the enhanced range of the surface charges' potential. In fact, as shown further in the text, there is no energetic well for the pair potential that corresponds to the PPO and the T-shaped configurations. Instead, we found an ever-increasing nonnegative potential energy as a function of the volume fraction. Consequently, no aggregationlike behavior is seen and the $g(r)$ for ρ=0.01 behaves as a simple fluid, as in the case of model *A* for the same value of λ. By increasing the volume fraction, a large $g(r)$ peak is developed that coincides with a not very pronounced $p(r)$ well. This indicates that the T-shaped configurations still appear, although the position of the peak in the radial distribution function is shifted to larger separations. This means that the platelets in this T-shaped configuration are not in contact any more, but separated as far as possible. Hence, this peak is shifted to the left as the concentration is increased. All these features are in high contrast with respect to the λ=1 nm case, in which the position of this first peak remains at a fairly constant distance of $\sim\sigma_{\perp}/2$. On the other hand, the peaks that characterize the PPO pair configurations are no longer present, indicating that these configurations have disappeared from the bulk. Finally, the small hump that signals the existence of very closed parallel configurations appears at a volume fraction value of 0.05, and is more clearly defined than in the corresponding values of ρ for the case λ=1 nm. As in the previous case, we can conclude that all these features are an effect of the packing of the system at high volume fraction values.

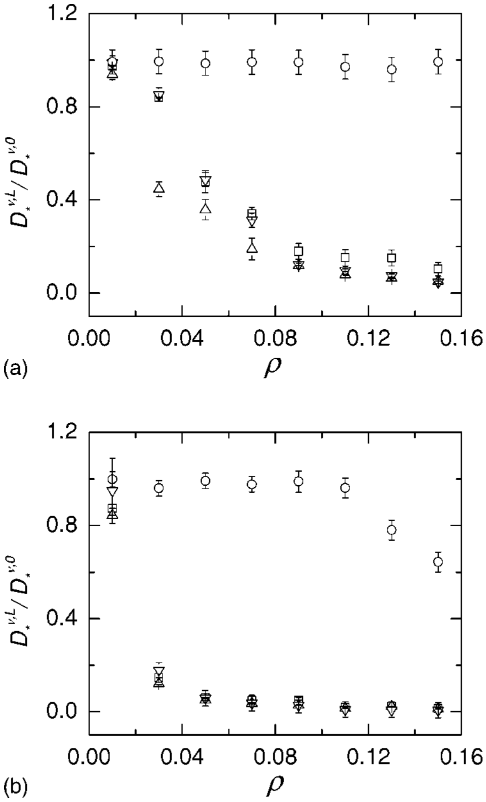

FIG. 11. Normalized SDC for model *A* with λ=1 nm (top) and λ=3 nm (bottom) as a function of ρ. $D_*^{\nu,L}$ were obtained from the asymptotic value of the fitting function [Eq. (27)]. The symbols in each figure correspond to $D_{\perp}^{T,L}$ (square), $D_{\parallel}^{T,L}$ (up triangle), $D_{\perp}^{R,L}$ (down triangle), and $D_{\parallel}^{R,L}$ (circle).

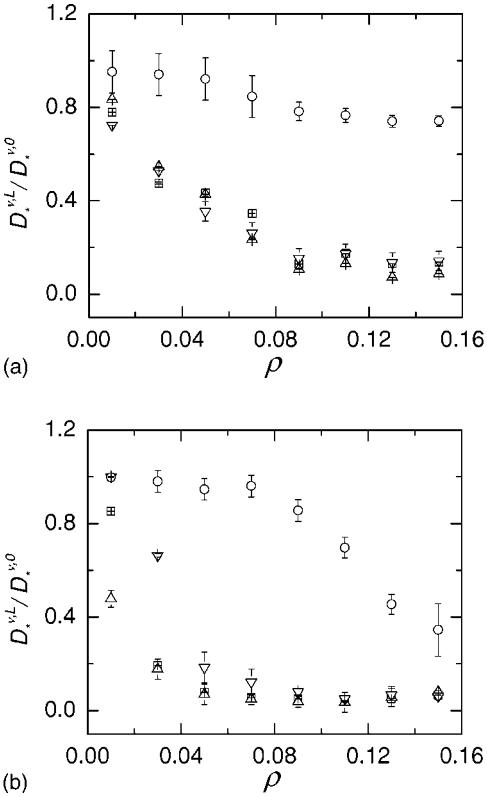

FIG. 12. Normalized SDC for model *B* with λ=1 nm (top) and λ=3 nm (bottom) as a function of ρ. $D_*^{\nu,L}$ were obtained from the asymptotic value of the fitting function [Eq. (27)]. The symbols in each figure correspond to $D_{\perp}^{T,L}$ (square), $D_{\parallel}^{T,L}$ (up triangle), $D_{\perp}^{R,L}$ (down triangle), and $D_{\parallel}^{R,L}$ (circle).

Self-diffusion coefficients

One of the purposes of this work is to present the results for the long-time self-diffusion coefficients (SDC's) of a

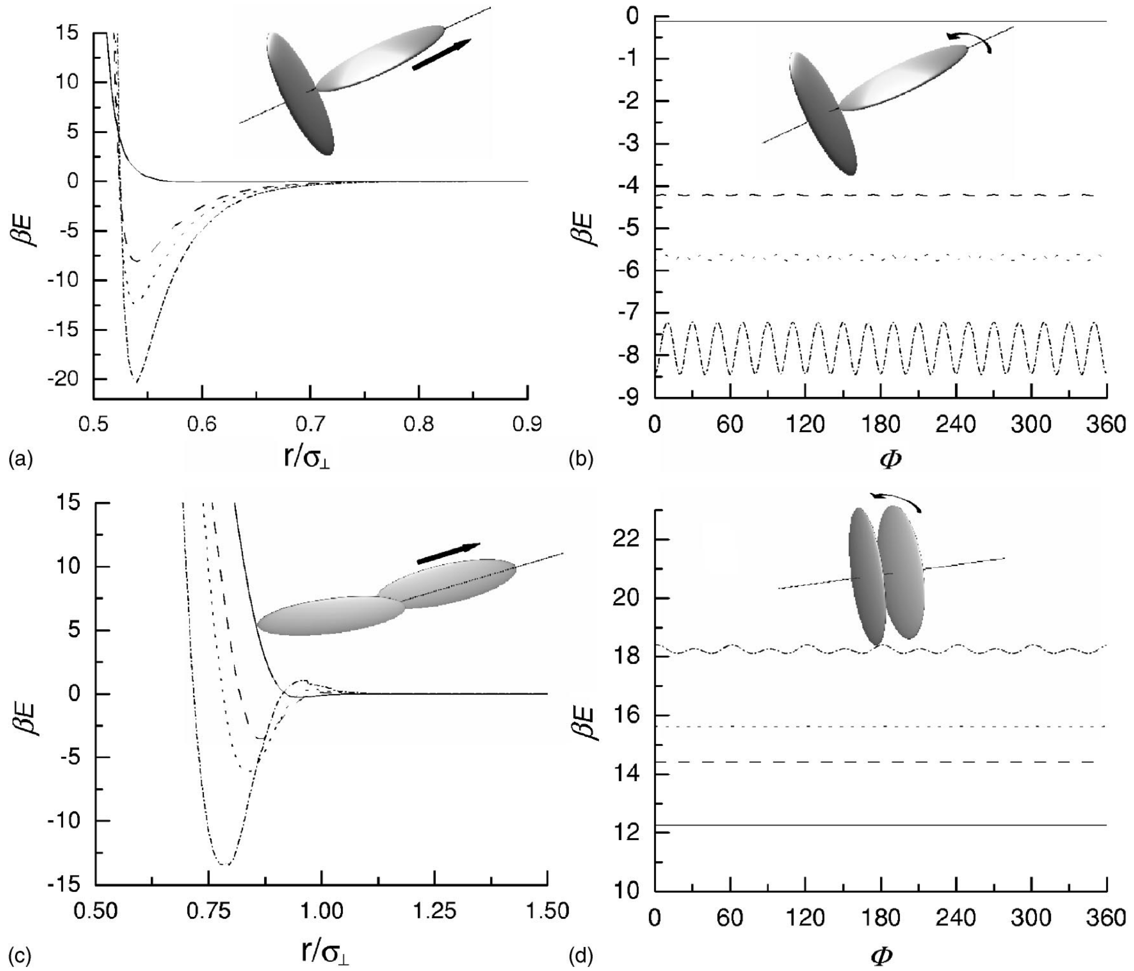

FIG. 13. Potential energy for two model B platelets with $\lambda = 1$ nm and for different configurations. (a) For a T-shaped configuration and as a function of the c.m.-c.m. distance. (b) For a T-shaped configuration and as a function of the rotation angle. (c) For a PPO configuration, with a fixed perpendicular projection of the c.m.-c.m. distance at 2.5 nm and as a function of the x projection of the c.m.-c.m. distance. (d) For a parallel configuration with a c.m.-c.m. distance of 6 nm and as a function of the rotation angle. The solid, dashed, dotted, and dashed-dotted lines correspond to $N_q = 469$, 91, 61, and 37, respectively. The total rim and superficial charges are kept constant.

tracer. The BD simulation of a tracer (that is governed by the direct interactions with the rest of the particles in the colloidal suspension) provides information of the self-diffusion process as a function of time through the calculation of the mean-square-displacement, namely,

$$W_*^T(t_M) \equiv \frac{1}{N}\sum_{\alpha=1}^{N}\left\langle\left|\sum_{m=1}^{M}\Delta R_{\alpha,*}^{(b)}(t_m)\right|^2\right\rangle,$$

$$W_*^R(t_M) \equiv \frac{1}{N}\sum_{\alpha=1}^{N}\left\langle\left|\sum_{m=1}^{M}\Delta \varphi_{\alpha,*}(t_m)\right|^2\right\rangle, \qquad (24)$$

where $* = \perp_x, \perp_y$, and $\parallel$. Thus, the time dependent SDC's are defined by

$$D_*^{\nu}(t_M) \equiv \frac{W_*^{\nu}(t_M)}{2t_M}, \qquad (25)$$

where $\nu = T, R$ and $t_M = M\Delta t$. In Fig. 10 we show, as an example, the time-dependent SDC's for a model B system with

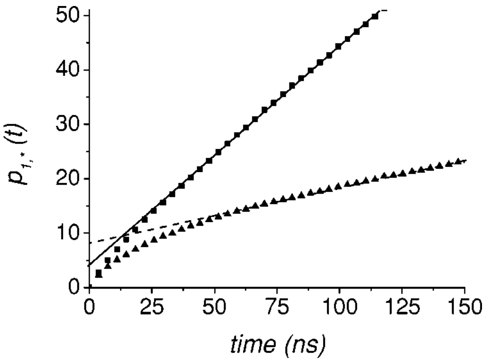

FIG. 14. Time evolution of the rotational correlation function $p_{1,*}$ for the same ρ and λ values used in Fig. 10. Solid and dashed lines are the least-squares, linear asymptotic fit to the data from which $D_{\perp}^{R,L}/D_{\perp}^{R,0}$ (triangles) and $D_{\parallel}^{R,L}/D_{\parallel}^{R,0}$ (squares) are computed.

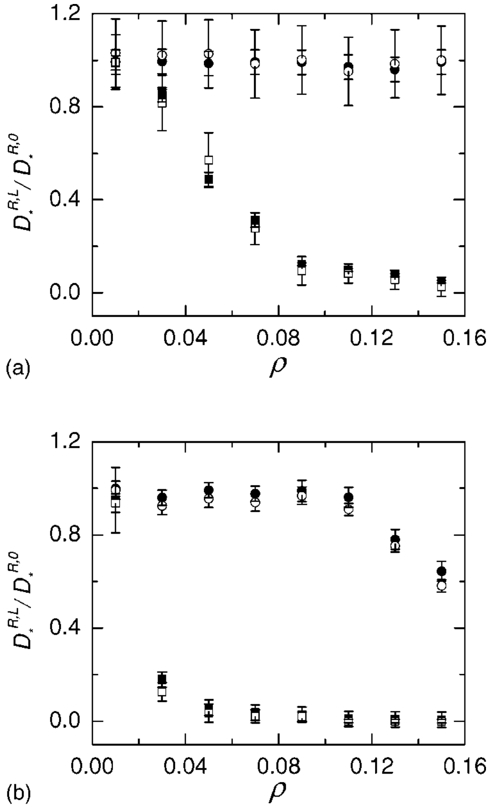

FIG. 15. Normalized rotational SDC's for model A with $\lambda=1$ nm (top) and $\lambda=3$ nm (bottom) as a function of the volume fraction ρ. Filled symbols correspond to SDC's computed from the asymptotic value of the fit to the function (27), whereas open symbols correspond to values computed from the slope of Eq. (30).

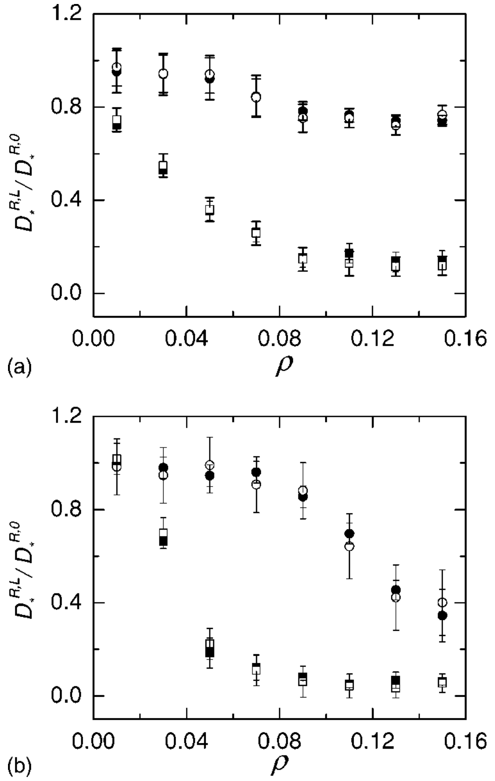

FIG. 16. Normalized rotational SDC's for model B with $\lambda=1$ nm (top) and $\lambda=3$ nm (bottom) as a function of the volume fraction ρ. Filled symbols correspond to SDC's computed from the asymptotic value of the fit to the function (27), whereas open symbols correspond to values computed from the slope of Eq. (30).

$\rho=0.13$ and $\lambda=1$ nm. These SDC's are normalized with the free-diffusion coefficients obtained in Sec. II C. In Fig. 10 we can observe a complex decreasing behavior for the different SDC's as a function of time. Its complexity is due to the direct interactions the tracer presents with the other platelets. In general, at long times the SDC's tend to a low finite value in the limit $t\to\infty$,

$$D_*^{\nu,L} = \lim_{t\to\infty} D_*^{\nu}(t). \tag{26}$$

In practice, the different values for the SDC's at long times were evaluated through an extrapolation procedure. This resource is necessary because the BD simulation only spans a small time interval. The procedure is based on the definition of a function that fits the simulation data and its value in the $t\to\infty$ limit is taken as the long-time SDC's. Several functions exist to adjust the simulation data [28,29]. Our proposal is

$$D_*^{\nu}(t) = D_*^{\nu,L} + A_*^{\nu}\exp[-(t/t_*^{\nu})^{\mu_*^{\nu}}], \tag{27}$$

where A_*^{ν}, t_*^{ν}, and μ_*^{ν} are fitting parameters. Note that $D_*^{\nu,L}$ is not considered as a fitting parameter because it is related to the free SDC's at short times $D_*^{\nu,0}=D_*^{\nu,L}+A_*^{\nu}$. In the Appendix, the values of all fitting parameters obtained for all systems are reported.

The normalized long-time SDC's $D_*^{\nu,L}/D_*^{\nu,0}$ computed from the fitting function [Eq. (27)] are displayed graphically in Figs. 11 and 12 for models A and B, respectively. It is observed in any of these figures that, in general, the long-time SDC's present a pronounced dependency on the volume fraction. As ρ increases, the value of these coefficients drops considerably. This effect is not surprising since the translational mobility of the particles is drastically reduced at high volume fraction values. Nevertheless, the very low SDC's found might point to gel formation. Note that these low SDC's are obtained for both models and for similar ρ values. In addition, it is also to be noted that a lower value of ρ is enough to produce such small values of the SDC's for higher λ. On the other hand, $D_{\parallel}^{R,L}/D_{\parallel}^{R,0}$ behaves quite differently. For model A and $\lambda=1$ nm, its value remains constant for all ρ studied, whereas for $\lambda=3$ nm, its value drops only at very large ρ values. In fact, this behavior was expected since rotations around the axis normal to the platelet surface should not change the free energy of the system, i.e., the platelets are free to make these movements because of their symmetry. Nevertheless, due to the charge discretization the platelets partially break their symmetry, and hence oscillations in the pair potential appear, as is shown in Figs. 13(b) and 13(d). The fact that $D_{\parallel}^{R,L}/D_{\parallel}^{R,0}$ decreases for $\lambda = 3$ nm is just due to the enhanced range of the repulsive potential. For the other normalized SDC's, it is seen that they present a similar behavior, i.e., they strongly decrease as the volume fraction increases. One should note that $D_{\perp}^{R,L}/D_{\perp}^{R,0}$ is affected in a similar way to that already observed for the translational SDC's. Obviously, movements around the x and y axes are strongly hindered for large concentrations. In particular, the value of $D_{\parallel}^{T,L}/D_{\parallel}^{T,0}$ is systematically lower than that of $D_{\perp}^{T,L}/D_{\perp}^{T,0}$ for $\lambda = 1$ nm in the entire ρ value range. This effect is explained by the fact that, as ρ increases, parallel configurations are favored, and so the mobility along the plane parallel to platelet surfaces is less hindered than the mobility perpendicular to that plane. For $\lambda = 3$ nm, however, this effect is no longer observed. Instead, it is seen from Fig. 11(b) that the ρ dependency is enhanced for all the translational coefficients.

As was already mentioned, the results of the long-time SDC's for model B are presented in Fig. 12. In general, similar features to model A are observed. That is, $D_{\parallel}^{R,L}/D_{\parallel}^{R,0}$ does not depend significantly on the volume fraction as the other SDC's do, and the dependency of the SDC's with ρ is more pronounced for $\lambda = 3$ nm. There are, however, some differences. Due to the fact that, for $\lambda = 1$ nm, the system aggregates even for the very diluted cases, the $D_{*}^{\nu,L}/D_{*}^{\nu,0}$ values are smaller than those corresponding to model A. This result is no longer valid for larger concentrations. Note that, for $\lambda = 1$ nm, $D_{\parallel}^{R,L}/D_{\parallel}^{R,0}$ is always smaller than one, which is a consequence of the potential energy oscillations of the T-shaped configuration for rotational movements around the z axis [see Fig. 13(b)]. For $\lambda = 3$ nm the effect is the same as that already observed in model A. Translational and rotational motion are hindered by the repulsion at high volume fractions, and so the corresponding SDC's decrease in comparison to their values for the $\lambda = 1$ nm case.

Comparison with other methods. In order to verify the validity of the employed method for calculating the rotational SDC's, we recalculate them by using a different one. This alternative method was originally employed in Ref. [20] for rodlike particles which interact via a two-site Yukawa potential. The rotational motion of disk-shaped particles, such as those studied in this work, can be conveniently characterized using the single-particle orientational time-correlation functions

$$C_{l,*}(t) = \langle P_l(\boldsymbol{e}_*(t) \cdot \boldsymbol{e}_*(0)) \rangle, \qquad (28)$$

where $P_l(x)$ is the lth Legendre polynomial and $\boldsymbol{e}_*$ is the vector along the principal axis ($* = \perp_x, \perp_y$, and $\parallel$). These functions are used to describe the light scattering data of a colloidal tracer particle [30]. For very dilute solutions the rotational motion is a pure diffusive process, so the Debye rotational diffusion equation is applicable. This leads to an exponentially decaying correlation function

$$C_{l,*}(t) = \exp[-l(l+1)D_{*}^{R,0}t]. \qquad (29)$$

Clearly, the potential interactions modify this purely exponential decay. Thus we study the first orientational correlation function that is obtained from Eqs. (28) and (29), namely,

$$p_{1,*}(t) = -\frac{\ln\langle P_1(t)\rangle}{2\,D_{*}^{R,0}t}. \qquad (30)$$

The time behavior of function $p_{1,*}(t)$, Eq. (30), which is plotted in Fig. 14, shows that initially this function increases linearly, with a slope value of 1, with time. Thus, for a very short time interval ($t < 5$ ns), the particles rotate as in a dilute solution. For very long times (not shown), the function $\langle P_1(t)\rangle$ deviates from the purely exponential decay and displays a complicated nonlinear behavior, which makes difficult to obtain quantitative predictions. However, for intermediate times the behavior is sufficiently smooth to allow a linear fit over a representative time interval. From Fig. 14 it is observed that, when passing from a regime of short times to a regime of intermediate times, a decrease of the slope from 1 to $D_{*}^{R,L}/D_{*}^{R,0}$ is obtained.

The coefficients $D_{\perp}^{R,L}/D_{\perp}^{R,0}$ and $D_{\parallel}^{R,L}/D_{\parallel}^{R,0}$, computed from the slope of $p_{1,*}(t)$ over a time interval that is highly dependent on the particular case studied, are compared with the corresponding coefficients obtained from the fitting function, Eq. (27), in Figs. 15 and 16 for models A and B, respectively. In these figures we can observe the agreement between both methods for all λ values studied. Now, for both models A and B, the error in $D_{\parallel}^{R,L}/D_{\parallel}^{R,0}$ computed from the slope of $p_{1,\parallel}(t)$ is always higher than the corresponding error computed from the asymptotic fit [Eq. (27)]. This behavior is more pronounced for values of $D_{\parallel}^{R,L}/D_{\parallel}^{R,0}$ close to 1.

IV. PAIR POTENTIAL ANALYSIS

In order to check the effect of discretizing the charge on the surface of the Laponite model, we carried out a pair potential analysis by considering several numbers of charged sites N_q. In particular, we present the results for model B and different pair configurations in Fig. 13. Here, Fig. 13(a) shows the pair potential energy for platelets in a T-shaped configuration as a function of the c.m.-c.m. separation and for $\lambda = 1$ nm. As can be seen, all curves present a minimum for distances slightly larger than $\sigma_{\perp}/2$ (even for the $N_q = 469$ case, although, its value is close to zero). The depth of the well, however, strongly depends on N_q. That is, if the charge discretization is increased, the depth of the energy well also increases. This effect is due to the large amount of charge per site at high discretization values, which allows a decrease in the energetic contribution of two unlikely charged sites close to each other, and also due to the fact that equally charged sites on the surfaces of the platelets become more separated.

For this same configuration the effect of the rotation on the potential energy as a function of the displacement angle is presented in Fig. 13(b). For all N_q values the potential is always attractive, although its strength greatly diminishes

TABLE I. Fitting parameters corresponding to model A, $\lambda = 1$, and 3 nm. t^{ν}_{*} is given in nanoseconds.

		$\lambda = 1$ nm			$\lambda = 3$ nm		
ρ	$\nu, *$	$A^{\nu}_{*}/D^{\nu,0}_{*}$	t^{ν}_{*}	μ^{ν}_{*}	$A^{\nu}_{*}/D^{\nu,0}_{*}$	t^{ν}_{*}	μ^{ν}_{*}
0.01	$T, \perp$	0.0242	84.82	0.9588	0.1258	43.90	0.9873
	$T, \parallel$	0.0609	310.2	0.5391	0.1560	47.83	1.2912
	$R, \perp$	0.0111	5.883	0.7234	0.0507	70.16	1.5426
	$R, \parallel$	0.0075	2.299	0.9442	0.0017	2.911	3.4551
0.03	$T, \perp$	0.1599	83.53	0.9603	0.8536	39.26	0.6429
	$T, \parallel$	0.5537	680.0	0.6372	0.8795	22.00	0.6011
	$R, \perp$	0.1482	77.82	0.9851	0.8214	114.3	0.6011
	$R, \parallel$	0.0059	2.065	2.5883	0.0832	3.929	4.5756
0.05	$T, \perp$	0.4904	251.0	0.6088	0.9383	13.54	0.5271
	$T, \parallel$	0.6423	79.76	0.6989	0.9494	5.407	0.4443
	$R, \perp$	0.5122	143.5	0.7444	0.9421	17.07	0.5583
	$R, \parallel$	0.0133	9.710	1.5725	0.0084	8.702	3.0645
0.07	$T, \perp$	0.6590	138.2	0.6135	0.9519	6.676	0.5018
	$T, \parallel$	0.8109	41.59	0.5870	0.9637	2.096	0.3980
	$R, \perp$	0.6872	76.84	0.6905	0.9630	6.632	0.5015
	$R, \parallel$	0.0079	12.35	0.7280	0.0233	1.069	6.1141
0.09	$T, \perp$	0.8205	75.46	0.6354	0.9503	3.969	0.5022
	$T, \parallel$	0.8814	18.30	0.5232	0.9720	1.037	0.3765
	$R, \perp$	0.8769	46.24	0.5827	0.9720	3.321	0.4857
	$R, \parallel$	0.0089	47.36	3.9826	0.0110	3.829	0.4329
0.11	$T, \perp$	0.8483	32.50	0.5856	0.9810	3.126	0.4404
	$T, \parallel$	0.9211	8.545	0.4670	0.9851	0.550	0.3244
	$R, \perp$	0.9020	20.17	0.5596	0.9904	1.983	0.4332
	$R, \parallel$	0.0286	4.232	8.7700	0.0385	6.653	0.9897
0.13	$T, \perp$	0.8496	93.25	0.5814	0.9767	2.180	0.4373
	$T, \parallel$	0.9366	22.01	0.4585	0.9781	0.358	0.3350
	$R, \perp$	0.9248	52.14	0.5412	0.9923	1.315	0.4240
	$R, \parallel$	0.0398	140.7	1.3027	0.2194	19.81	0.5954
0.15	$T, \perp$	0.8971	12.35	0.5863	0.9854	1.794	0.4225
	$T, \parallel$	0.9488	2.528	0.4440	0.9882	0.208	0.2988
	$R, \perp$	0.9525	6.126	0.5170	0.9939	0.850	0.4116
	$R, \parallel$	0.0073	0.982	1.3570	0.3614	8.074	0.6945

with an increasing N_q value. Furthermore, the potential curves oscillate around given mean values. Note that the number of maxima and minima coincides with the number of rim sites. Naturally, the oscillations are more pronounced as the number of sites is reduced. For $N_q = 469$, the oscillations turn almost negligible. These oscillations in the pair potential, which lead to a symmetry breaking, explain the decrease of $D^{R,L}_{\parallel}/D^{R,0}_{\parallel}$ with an increasing platelet concentration.

As previously seen, model B presents another type of arrangement that was found to be present in the system bulk. This is the PPO configuration which is considered in Fig. 13(c). Here, the pair potential is plotted against the x projection of the c.m.-c.m. distance. As can be seen, the curves show an attractive well in the potential located at a separation slightly larger than $0.75\sigma_{\perp}$. At this position, the rim charges of one platelet are faced to the surface charges of the other and vice versa, creating a minimum in the configurational potential energy. For a separation of $\approx \sigma_{\perp}$ the potential has a repulsive hump, which is explained by the fact that, at this distance, the rim charges of both platelets are at the closest possible distance. As in the case of the T-shaped configuration, increasing N_q diminishes the depth of the attractive well and shifts its location to larger separation values. It is important to note that, even for $N_q = 469$, there is still an attractive well in the potential, but with a very small depth.

It should be mentioned that the attractive wells shown in Figs. 13(a) and 13(b) are enhanced for smaller values of λ, higher values of Q_T, and higher ring charges. Even for $N_q = 469$, deep wells are obtained if the parameters are somewhat changed. In particular, we obtain a 8 k_BT depth well in Fig. 13(a) for $Q_T = 850$ e, $\lambda = 0.8$ nm, and a positive ring charge equal to 0.12 Q_T, which is not very far from the one

TABLE II. Fitting parameters corresponding to model *B*, $\lambda=1$, and 3 nm. t_*^ν is given in nanoseconds.

		$\lambda=1$ nm			$\lambda=3$ nm		
ρ	$\nu,*$	$A_*^\nu/D_*^{\nu,0}$	t_*^ν	μ_*^ν	$A_*^\nu/D_*^{\nu,0}$	t_*^ν	μ_*^ν
0.01	$T,\perp$	0.2212	8.930	0.4607	0.1474	161.7	1.2934
	$T,\parallel$	0.1657	2.637	0.6856	0.5217	476.2	0.8386
	$R,\perp$	0.2770	33.22	0.4914	0.0009	81.30	0.7990
	$R,\parallel$	0.0485	3.961	0.4954	0.0028	12.31	0.6234
0.03	$T,\perp$	0.5244	24.04	0.3555	0.8083	63.68	0.7197
	$T,\parallel$	0.4546	7.775	0.3779	0.8228	64.77	0.6607
	$R,\perp$	0.4721	41.60	0.4315	0.3369	163.7	1.0156
	$R,\parallel$	0.0596	3.011	0.7148	0.0201	71.84	3.0404
0.05	$T,\perp$	0.5269	13.55	0.4409	0.9217	19.61	0.5808
	$T,\parallel$	0.5726	9.605	0.3330	0.9301	15.83	0.5480
	$R,\perp$	0.6460	87.40	0.4581	0.8157	125.5	0.7118
	$R,\parallel$	0.0789	12.47	1.0297	0.0539	32.21	0.746
0.07	$T,\perp$	0.6565	7.775	0.4257	0.9459	7.814	0.5168
	$T,\parallel$	0.7664	11.13	0.3264	0.9506	5.278	0.4963
	$R,\perp$	0.7371	22.87	0.4237	0.8778	28.77	0.6043
	$R,\parallel$	0.1541	3.028	0.7360	0.0329	7.624	1.0595
0.09	$T,\perp$	0.8708	13.86	0.3474	0.9503	3.652	0.4945
	$T,\parallel$	0.8932	11.59	0.3150	0.9625	2.217	0.4389
	$R,\perp$	0.8467	19.70	0.4082	0.9191	9.205	0.5569
	$R,\parallel$	0.2176	5.780	0.6744	0.1444	7.349	0.6307
0.11	$T,\perp$	0.8263	7.599	0.4285	0.9580	2.020	0.4767
	$T,\parallel$	0.8684	6.206	0.3689	0.9647	1.088	0.4399
	$R,\perp$	0.8274	12.64	0.4532	0.9493	4.505	0.5121
	$R,\parallel$	0.2343	6.095	0.7188	0.3029	4.356	0.6867
0.13	$T,\perp$	0.8694	6.506	0.4570	0.8292	0.721	0.6587
	$T,\parallel$	0.9284	4.416	0.3742	0.9429	0.553	0.4751
	$R,\perp$	0.8651	11.57	0.4626	0.9320	2.035	0.5287
	$R,\parallel$	0.2596	11.39	0.6312	0.5453	3.273	0.6622
0.15	$T,\perp$	0.8633	4.209	0.4696	0.8332	0.453	0.6559
	$T,\parallel$	0.9132	1.978	0.4191	0.9197	0.296	0.5402
	$R,\perp$	0.8579	6.679	0.4994	0.8209	1.500	0.6359
	$R,\parallel$	0.2587	6.028	0.9539	0.5650	1.473	0.6476

obtained for $N_q=61$. We should remark that the surface and ring charges of Laponites vary depending on the way they are synthesized [7], and so, these other parameters and the 61 sites model are still representative of a Laponite particle.

Figure 13(d) reports the variation of the potential energy as a function of the rotational displacement between two model *B* parallel platelets. The interaction is dominated by the repulsion of the equally charged sites in both platelets. However, for rotational displacements of one platelet with respect to the other, the effect of the charge discretization is seen again as an oscillation of the potential around a mean value. The maximum value of the oscillations corresponds to an arrangement in which the rim charges of the two platelets are closest, and the minimum to the opposite case. Since the platelets are more separated than in the case of the T-shaped configuration, the oscillations are less pronounced. Indeed, they are almost imperceptible for not so large values of N_q. These oscillations explain the slight decrease of $D_\parallel^{R,L}/D_\parallel^{R,0}$ for model *A* $\lambda=3$ nm, where no T-shaped configurations are present.

Although it is not shown, a similar analysis was performed for the $\lambda=3$ nm case. Here, the effective range of the potential is greatly extended, leading to strong effects in the pair interaction between platelets if compared with the $\lambda=1$ nm case. Here, we observed that the potential well disappeared for both the T-shaped and PPO configurations, and for all N_q values considered. This explains the result of an ever-increasing system energy as a function of the volume fraction for this case.

In model *A*, the potential energy is purely repulsive, and a pair configuration of parallel platelets is favored, since this type of arrangement avoids the closeness of sites, and hence lowers the potential energy. This is why we omitted a detailed study of the pair potential of this model.

V. CONCLUSIONS

In this paper we presented a systematic study of two simple models for a synthetic clay by means of BD simulations. These models mimic the Laponite's charge behavior when dispersed by a solvent at different *p*H conditions. Hence, a model with equally charged sites, model *A*, and another with rim charges of opposite sign, model *B*, were considered. Static and dynamic properties were studied for both models for two different values of the Debye length and several volume fractions that span a wide range of concentrations.

Our results reproduce to a great extent the complex mesostructure and rich phase behavior previously reported for similar models studied by MD simulations [15]. However, due to the addition of several sort-range repulsive sites that impede the interpenetration of the platelets, our simulations predict another nonreported type of configuration for model *B*. This is a parallel, partially overlapped arrangement in which the rim charges of one platelet are faced to the surface charges of the other and vice versa. As shown in Sec. IV, this configuration also shows an energetic well when plotted against the c.m.-c.m. distance between platelets. This well, and the one yielded for the T-shaped configuration, explains why the system's energy decreases with increasing platelet concentration up to a given volume fraction. For concentrations over this volume fraction, the tendency is reversed due to the appearance of crowded parallel configurations. This exemplifies the complex behavior of this kind of system.

On the other hand, the BD technique allows the proper study of time dependent SDC's from which the asymptotic SDC's are extrapolated. This was done by two different methods which yield very similar values, and hence, corroborate the physical relevance of the results. As expected, the SDC's are strongly influenced by the structure of the suspension. For example, for those systems with a preferential parallel structure, the translation parallel to the axial axis of each platelet (normal to the platelet surface) is most hindered. In addition, it was shown that increasing the Debye length or increasing the platelet concentration leads to a reduction of the SDC's. This reduction is quite large for large enough volume fractions, suggesting the formation of a gel phase. The only exception was seen for the SDC associated with rotations around the axial axis. This SDC diminishes only when the effect of the charge discretization becomes important.

We would like to point out that considering just 61 charged sites to model the charged surface of the Laponite particles is nowadays a necessary simplification, due to the computational effort that would surely lead to qualitative discrepancies with the predictions of a model having 700 charged sites and the same parameters. This is supported by the analysis performed in Sec. IV. On the other hand, if parameters such as the surface charge, edge charge, and Debye length are allowed to change for obtaining a match between both pair potentials, similar results are expected from the models based on 61 and 700 charged sites.

Finally, this work can be seen as a step along the way towards the study of other interesting properties, such as viscosity. This property is very important for practical purposes such as well drilling operations.

ACKNOWLEDGMENT

This work was supported by Instituto Mexicano del Petróleo through Grant Nos. D.00324 and D.00072.

APPENDIX: FITTING PARAMETERS

In Tables I and II, the values of the fitting parameters of Eq. (27) to the long-time SDC are presented for the different systems studied.

---

[1] H. van Olphen, *An Introduction to Clay Colloid Chemistry* (National Academy of Sciences, Washington, D.C., 1977).
[2] C. E. Weaver and L. D. Pollard, *The Chemistry of Clay Minerals* (Elsevier, Amsterdam, 1973).
[3] B. Rand, E. Pekenc, J. W. Goodwin, and R. W. Smith, J. Chem. Soc., Faraday Trans. 1 **76**, 225 (1980).
[4] R. Sohm and T. F. Tadros, J. Chem. Soc., Faraday Trans. 1 **85**, 225 (1989).
[5] A. Mourchid, E. Lécolier, H. Van Damme, and P. Levitz, Langmuir **14**, 4718 (1998).
[6] A. Mourchid, A. Delville, J. Lambard, E. Lécolier, and P. Levitz, Langmuir **11**, 1942 (1995).
[7] J. M. Saunders, J. W. Goodwin, R. M. Richardson, and B. Vincent, J. Phys. Chem. B **103**, 9211 (1999).
[8] J. C. P. Gabriel, C. Sanchez, and P. Davidson, J. Phys. Chem. **100**, 11 139 (1996).
[9] M. Kroon, G. H. Wegdam, and R. Sprik, Europhys. Lett. **35**, 621 (1996).
[10] T. Nicolai and S. Cocard, Langmuir **16**, 8189 (2000).
[11] F. Chou Chang, N. T. Skipper, and G. Sposito, Langmuir **11**, 2734 (1995).
[12] M. Chávez-Páez, K. Van Workum, L. de Pablo, and J. J. de Pablo, J. Chem. Phys. **114**, 1405 (2001).
[13] E. J. M. Hensen and B. Smit, J. Phys. Chem. B **106**, 12 664 (2002).
[14] G. Odriozola and F. de J. Guevara-Rodríguez, Langmuir **20**, 2010 (2004).
[15] S. Kutter, J. P. Hansen, M. Sprik and E. Boek, J. Chem. Phys. **112**, 311 (2000).
[16] M. Dijkstra, J. P. Hansen, and P. A. Madden, Phys. Rev. Lett. **75**, 2236 (1995).
[17] D. L. Ermack, J. Chem. Phys. **62**, 4189 (1975).
[18] H. Löwen, Phys. Rev. E **50**, 1232 (1994).
[19] E. Dickinson, J. Chem. Soc., Faraday Trans. 2 **81**, 591 (1985).
[20] A. C. Brańka and D. M. Heyes, Phys. Rev. E **50**, 4810 (1994).
[21] A. C. Brańka and D. M. Heyes, J. Chem. Phys. **109**, 312

(1998).
[22] R. Ying and M. H. Peters, J. Chem. Phys. **91**, 1287 (1989).
[23] C. H. Cho, J. Urquidi, and G. W. Robinson, J. Chem. Phys. **111**, 10171 (1999).
[24] J. García de la Torre and V. Rodes, J. Chem. Phys. **79**, 2454 (1983).
[25] F. Perrin, J. Phys. Radium **7**, 1 (1936).
[26] H. Shimizu, J. Chem. Phys. **37**, 765 (1962).
[27] M. P. Allen and D. J. Tildesley, *Computer Simulation of Liquids* (Clarendon Press, New York, 1987).
[28] H. Löwen, J. Phys.: Condens. Matter **4**, 10105 (1993).
[29] G. Nägele, M. Medina-Noyola, R. Klein, and J. L. Aruaz-Lara, Physica A **149**, 123 (1988).
[30] B. J. Berne and R. Pecora, *Dynamic Light Scattering* (Wiley, New York, 1976).